NATIONAL ENERGY TECHNOLOGY LABORATORY

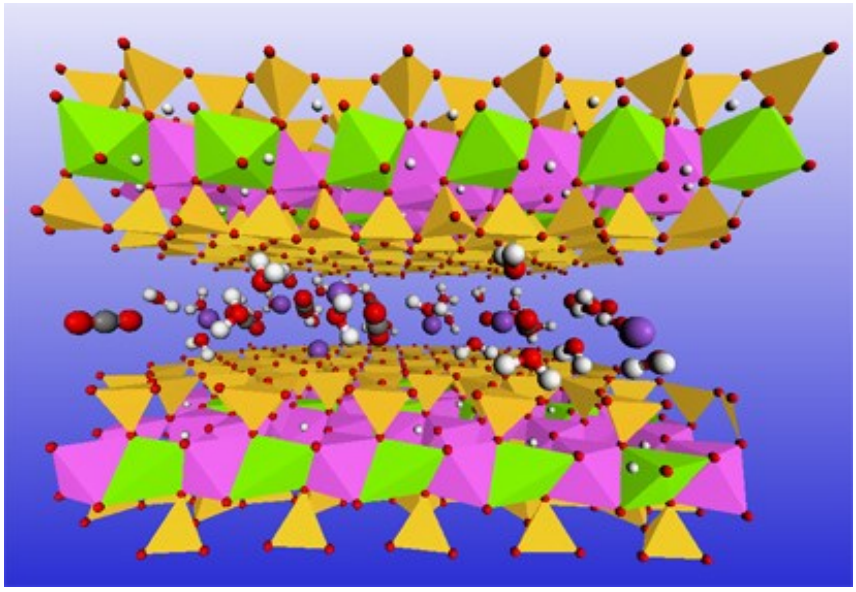

Molecular Simulation Models of Carbon Dioxide Intercalation in Hydrated Sodium Montmorillonite

X June 2016

U.S. DEPARTMENT OF ENERGY

Office of Fossil Energy

NETL-TRS-X-2016

Disclaimer

Cover Illustration: Schematic representation of the clay/water/CO_2 system.

Suggested Citation: Myshakin, E.; Saidi, W.; Romanov, V.; Cygan, R.; Jordan, K.; Guthrie, G. *Molecular Simulation Models of Carbon Dioxide Intercalation in Hydrated Sodium Montmorillonite*; NETL-TRS-X-2016; NETL Technical Report Series; U.S. Department of Energy, National Energy Technology Laboratory: Morgantown, WV, 2016; p 40.

An electronic version of this report can be found at:

http://www.netl.doe.gov/research/on-site-research/publications/featured-technical-reports

https://edx.netl.doe.gov/carbonstorage

Molecular Simulation Models of Carbon Dioxide Intercalation in Hydrated Sodium Montmorillonite

Evgeniy Myshakin[1,2], Wissam Saidi[3], Vyacheslav Romanov[1], Randall Cygan[4], Kenneth Jordan[1,5], George Guthrie[6]

[1] U.S. Department of Energy, National Energy Technology Laboratory, 626 Cochrans Mill Road, Pittsburgh, PA 15236

[2] U.S. Department of Energy, National Energy Technology Laboratory, AECOM Corporation, 626 Cochrans Mill Road, Pittsburgh, PA 15236

[3] Department of Chemical and Petroleum Engineering, University of Pittsburgh, 1249 Benedum Hall, 3700 O'Hara Street, Pittsburgh, PA 15261

[4] Sandia National Laboratories, 1515 Eubank SE, Albuquerque, NM 87185

[5] Department of Chemistry, University of Pittsburgh, Chevron Science Center, 219 Parkman Avenue, Pittsburgh, PA 15260

[6] Los Alamos National Laboratory, Bikini Atoll Road, SM 30, Los Alamos, NM 87545

NETL-TRS-X-2016

X June 2016

NETL Contacts:

Vyacheslav Romanov, Principal Investigator

Angela Goodman, Technical Portfolio Lead

Cynthia Powell, Executive Director, Research and Innovation Center

This page intentionally left blank.

Table of Contents

List of Figures

List of Tables

Acronyms, Abbreviations, and Symbols

Term	Description
3-D	Three-dimensional
Å	Angstrom
B3LYP	Becke-3-parameter-Lee-Yang-Parr potential
BOMD	Born-Oppenheimer molecular dynamics
CCSD(T)	Coupled-cluster with single and double (triple) electron excitations
DFT	Density functional theory
DRIFTS	Diffuse reflectance infrared Fourier-transform spectroscopy
DZVP	Split-valence double-zeta basis set with polarizable functions
fs	Femtosecond
Γ point	A center point of a fundamental region (Brillouin zone) of wave vectors propagating through a crystal lattice
EMP2	Force field for carbon dioxide
GPW	Gaussian-plane wave scheme
LJ	Lennard-Jones
MC	Monte-Carlo
MD	Molecular dynamics
MMT	Montmorillonite
NETL	National Energy Technology Laboratory
NMR	Nuclear magnetic resonance
NPT	Isobaric-isothermal ensemble
NVT	Canonical ensemble
PPPM	Particle-particle particle-mesh method
ps	Picosecond
RDF	Radial distribution function
$scCO_2$	Supercritical carbon dioxide
SPC	Force field for water
STx	Montmorillonite samples from Texas
SWy	Montmorillonite samples from Wyoming
TOT	Tetrahedral-octahedral-tetrahedral
VACF	Velocity autocorrelation function
W	Water
XRD	X-ray diffraction

Acknowledgments

This work was completed as part of National Energy Technology Laboratory (NETL) research for the U.S. Department of Energy's (DOE) Carbon Storage Program.

The authors wish to acknowledge Grant Bromhal and Brian Strazisar for programmatic guidance, direction, and support.

EXECUTIVE SUMMARY

Carbon capture and storage (CCS) technologies provide effective options for reducing carbon dioxide (CO_2) emissions and mitigating global climate change. Geologic CO_2 storage involves the injection of supercritical CO_2 into deep geologic formations overlain by sealing formations and geologic traps that prevent the CO_2 from escaping. The ability of seals to retain injected CO_2 depends on their permeability and geomechanical property evolution. Caprocks are often comprised of shale or mudstone enriched with swelling clay minerals that can expand or contract upon interaction with CO_2. Intercalation of CO_2 into interlayer of swelling clay causes evolution of the geomechanical stress and can promote fracture formation. The interlayer of expanded clay provides ample space for additional permanent CO_2 storage and its subsequent transformation into carbonates.

To evaluate the effectiveness of such CO_2 storage scenarios and to better understand multiphase flow in storage reservoirs and seals, for improved injectivity and trapping, investigators working at the National Energy Technology Laboratory (NETL) are conducting research to develop insights into important aspects of CO_2 interactions with mineral surfaces, CO_2 storage capacity and trapping mechanisms in clays as well as induced changes in geomaterials properties and diffusion rates.

This report provides a detailed description of results of theoretical work completed to date and preliminary discussion of findings and insights; and reports the results from CO_2-clay interactions modeling runs.

In this study, classical molecular dynamics simulations and density functional theory (DFT)-based molecular dynamics are used to elucidate the process of CO_2 intercalation into hydrated Na-montmorillonite at *P-T* conditions relevant to geological formations suitable for CO_2 storage. Of particular interest are the structural and transport properties of interlayer species after CO_2 intercalation. The conducted simulations allowed the research team to quantify expansion/contraction of smectite as a function of CO_2 and H_2O compositions. The resulting swelling curves can be used to gauge the amount of stored CO_2, compare it to the experiment, and estimate changes in geomechanical properties of the storage formation. The obtained results showed that the infrared signal of the asymmetric stretch vibration of CO_2 molecule is extremely sensitive to the solvent environment. The extent of the frequency shift relative to the gas-phase value can be used to probe hydration level in the interlayer with intercalated CO_2. Interaction of supercritical CO_2 with brine in deep geological formations promotes an increase of hydrophobicity of clay surfaces. As a result of wettability alteration, estimated diffusion constants of CO_2 and H_2O increase with the increased CO_2 load; this can contribute to faster migration of CO_2 throughout the formation.

1. REVIEW OF EXPERIMENTAL AND THEORETICAL PAPERS DEVOTED TO CARBON DIOXIDE INTERCALATION INTO SMECTITE CLAY MINERALS

Long-term storage of industrial carbon dioxide (CO_2) in subsurface geological strata is considered a viable option for mitigating greenhouse gas emission (NETL, 2013). The technology of geologic CO_2 storage involves the injection of supercritical CO_2 ($scCO_2$) into deep geologic formations such as saline aquifers overlain by sealing caprocks and geologic traps that would prevent the CO_2 from escaping. The ability of seals to retain injected CO_2 depends on their permeability and geomechanical property evolution (Allen and Allen, 2005). Caprocks are often comprised of shale or mudstone enriched with clay minerals, including swelling clays like montmorillonite (MMT) (Abdou and Ahmaed, 2010). MMT is a layered aluminosilicate where the central sheet is composed of octahedrally coordinated aluminum (Al) atoms, and the adjacent sheets contain tetrahedrally coordinated silicon (Si) atoms. These sheets comprise a 2:1 or tetrahedral-octahedral-tetrahedral (TOT) layer. In MMT, the TOT layers are negatively charged due to substitution of divalent metals (e.g., Mg^{2+} or Fe^{2+}) for the octahedrally coordinated Al or by less common substitution of Al for Si at tetrahedral sites. Hydroxyl groups complete the coordination of each octahedra. The negative charge of the TOT layers is counterbalanced by interlayer cations (e.g., Na^+, Li^+, Ca^{2+}) that are usually hydrated allowing for expansion or contraction of the interlayer distance of the clay depending on the relative humidity (Fu et al., 1990). Swelling clay particles interacting with $scCO_2$ can also undergo changes in interlayer content and in the basal spacing (Giesting et al., 2012; Schaef et al., 2012). This can lead to changes in porosity, permeability, and formation of micro fractures in caprocks. As a result, studies of the interactions between $scCO_2$ and the minerals of caprocks are necessary for assessing impacts for the long-term exposure of injected CO_2 to geological seals (Kwak et al., 2011).

Dry $scCO_2$ injected into a geological aquifer will become hydrated as a result of contact with brine retained at mineral surfaces and nanopores (Spycher et al., 2003). The resulting hydrated CO_2 interacts with the caprocks predominantly through diffusion unless pre-existing or evolved fractures provide pathways for CO_2 migration (Gaus, 2010). Recently, Giesting et al. (2012) reported in situ X-ray diffraction (XRD) characterization of gaseous CO_2 and $scCO_2$ interacting with Na-rich-MMT at T = 45 °C and P = 50–650 bar (in experiments, Na-rich-MMT is typically represented by natural or Na-exchanged SWy montmorillonite samples from Wyoming, and Ca-rich-MMT by natural or Ca-exchanged STx montmorillonite samples from Texas. In addition to the prevailing interlayer cations there are differences in the distributions of Mg, Al, and Si within the silicate layers of SWy and STx clay samples, which may complicate interpretation of the results (Costanzo, 2001; Martin, 1979)). The study by Giesting et al. (2012) showed that for partially-hydrated samples the spacing between the mineral layers (basal *d*-spacing) expands upon CO_2 adsorption and that the degree of expansion depends on the initial water content in the interlayers. In the absence of CO_2, the basal *d*-spacing is around 10 Å for nearly dry clay (the 0W hydration state) and increases to 12.5 Å for a fully saturated monolayer water arrangement (the 1W hydration state characterized with basal *d*-spacings in the range of 11.5–12.5 Å) (Fu et al., 1990; Cygan et al., 2004; Marry et al., 2002). Upon incorporation of more water, the *d*-spacing can increase to 14.5–15.5 Å to the next stable state where water forms a bilayer structure (the 2W hydration state) (Fu et al., 1990; Cygan et al., 2004; Marry et al., 2002). The XRD measurements showed that nearly dry clay displays no significant response upon exposure to dry $scCO_2$ and that residual water is required to intercalate CO_2.

Maximum expansion upon CO_2 intercalation was found at initial d = 11.3 Å resulting in swelling to d = 12.5 Å, the value that corresponds to the 1W state. The in situ XRD study by Schaef et al. (2012) on $scCO_2$ interacting with Ca-MMT at submonolayer water content confirms the expansion of the clay phase to d values corresponding to the 1W state after exposure to dry $scCO_2$ over a range of temperatures (50–100 °C) and pressures (90, 125, and 180 bar). Interaction of dry $scCO_2$ with smectite clay in the 2W state results in a collapse of the d-spacing to that of the 1W state (Schaef et al., 2012). However, interaction of Na-exchanged SWy and Ca-exchanged STx samples with variably wet $scCO_2$ (2–100% saturation of H_2O) at T = 50 °C and P = 90 bar can lead to swelling even to the values equal to the 3W state with a d-spacing of 18.8 Å (Schaef et al., 2012; Ilton et al., 2012). Thus, dry $scCO_2$ has the capacity to dehydrate clay and to promote increase of seal permeability due to clay collapse. On the other hand, the presence of water in $scCO_2$ can facilitate further swelling of clay.

Loring et al. (2012) further confirmed intercalation of CO_2 by means of nuclear magnetic resonance (NMR) spectroscopy and attenuated total reflection infrared spectroscopy. They found that intercalated CO_2 molecules are rotationally constrained and do not appear to react with waters to form bicarbonate or carbonic acid (Loring et al., 2012). Using diffuse-reflectance infrared spectroscopy, Romanov et al. (2010a,b), Romanov (2013), and Hur et al. (2013) have analyzed the vibrational fingerprint of CO_2 trapped in SWy and STx samples and also concluded that CO_2 can be intercalated in the interlayers of smectite minerals. These experiments revealed 5–10 cm^{-1} red shifts of the asymmetric stretch fundamental frequency for the trapped CO_2 relative to that of the gas-phase molecule (Romanov, 2013). CO_2 trapped in clay interlayers is in an intricate environment involving interactions with interlayer ions, water, and clay surfaces. As was shown by Duncan and co-workers (Gregoire and Duncan, 2002; Walker et al., 2003; Jaeger et al., 2004) the asymmetric stretch fundamental of CO_2 is shifted 10–80 cm^{-1} to the blue when the molecule forms a complex with metal ions. This observation suggests that it is the interaction with water and/or internal clay surfaces that is responsible for the observed red shift of the asymmetric stretch of CO_2 in interlayers of MMT.

Recently, Botan et al. (2010) performed Monte-Carlo (MC) and molecular dynamics (MD) simulations of CO_2 intercalation into Na-MMT using a force field for clay from Smith (1998) and the force field for water (SPC) (Berendsen et al., 1981) and the force field for CO_2 (EMP2) (Harris et al., 1995) models for water and carbon dioxide, respectively. Specifically, they considered Na-MMT in equilibrium with H_2O-CO_2 mixtures at T = 75 °C, and P = 25 and 125 bar. Their simulations indicated that hydrated clay can intercalate CO_2 and that the thermodynamically stable structures are characterized with basal d-spacings corresponding to the 1W and 2W hydration states. That is consistent with the experiment which shows that exposure of MMT to CO_2 resulted in expansion of clay particles giving the basal d-spacings equal to those values at 1W or 2W (Giesting et al., 2012; Schaef et al., 2012). Monte Carlo simulations of non-hydrated Na-MMT clay in equilibrium with dry $scCO_2$ have shown that CO_2 intercalation is unfavorable until large d-spacing distances (>2W) (Yu and Yang, 2011). For d-spacings >15.5 Å, the Helmholtz free energy displays a set of closely-spaced local minima separated by small barriers (Yu and Yang, 2011). Other modeling studies (Yang and Zhang, 2005; Peng et al., 2007; Cole et al., 2010) using different force fields, also indicate that CO_2 molecules can exist in the interlayers of clay minerals. At the same time, little is known about the molecular details of CO_2 intercalation in the interlayer of smectite clays.

In the present study, classical molecular dynamics simulations are used to elucidate the process of CO_2 intercalation into hydrated Na-MMT at initial H_2O content and *P*-*T* conditions relevant to geological formations for CO_2 storage. Of particular interest are the structural and transport properties of interlayer species after CO_2 intercalation. In addition, density functional theory (DFT)-based molecular dynamics is engaged to compute vibrational power spectra for comparison with the experimental IR spectra and the power spectra from force field simulations.

2. COMPUTATIONAL DETAILS

2.1 MOLECULAR DYNAMICS SIMULATIONS USING DENSITY FUNCTIONAL THEORY (DFT)

In recent years, computational resources have improved making it possible to tackle complex clay mineral systems by using electronic structure methods. DFT, in particular, provides reliable estimates of electrostatic potentials, thermodynamics, spectroscopic data, reaction mechanisms, and other properties (Cygan et al., 2009; Sholl and Steckel, 2009). DFT-based Born-Oppenheimer molecular dynamics (BOMD) simulations were carried out using the CP2K software package (CP2K, 2013). The evolution of a system using BOMD methods is governed by Newtonian dynamics with energies and forces at each time step being estimated from DFT calculations (Marx and Hutter, 2009). Goedecker-Teter-Hutter pseudopotentials (Goedecker et al., 1996; Krack, 2005) were used together with a hybrid Gaussian-plane wave scheme (GPW) with a split-valence double-zeta basis set with polarizable functions (DZVP) quality Gaussian basis set (VandeVondele and Hutter, 2007) for the Kohn-Sham orbitals and an energy cutoff of 350 Rydbergs for the plane-wave expansion of the electron density. The gradient-corrected correlation functional of Perdew et al. (1996) was employed, together with the DFT-D2 method (Grimme, 2006) to include long-range, two-body dispersion corrections (previous studies by Voora et al. (2011) and Zhang et al. (2012) demonstrated the importance of such corrections). In the DFT-D2 scheme (Grimme, 2006) dispersion-corrections are described in terms of damped atom-atom $C_6^{AB} \cdot R^{-6}_{AB}$ terms, where R_{AB} is the distance between atoms A and B. A damping factor is engaged to avoid double counting and divergence at small R_{AB} (Tkatchenko and Scheffler, 2009). The C_6^{AB} coefficients for describing dispersion between different atom types are defined in terms of the C_6^{AA} and C_6^{BB} coefficients by using the Lorentz-Bertholet combination rule (Allen and Tildesley, 1987).

The supercell for Na-MMT was developed starting from the structure of pyrophyllite (Lee and Guggenheim, 1981) which has no metal cation substitution and thus has neutral layers. A unit cell with $[Al_4O_8(OH)_4(Si_8O_{12})]$ composition was used for pyrophyllite. The lattice parameters of the unit cell are: a = 5.16 Å, b = 8.97 Å, and c = 9.37 Å, and α = 91.5º, β = 100.5º and γ = 89.6º (Lee and Guggenheim, 1981). To prepare the MMT structural model, a triclinic 2 x 1 x 1 supercell with one isomorphic octahedral Al^{3+}/Mg^{2+} substitution per unit cell was employed. This introduces one negative charge for each $O_{20}(OH)_4$ unit, which is compensated by an Na^+ ion in the interlayer space. This produces a supercell with the formula $Na_2[MgAl_3O_8(OH)_4(Si_8O_{12})]_2$. The Γ point sampling of the Brillouin zone is adequate because of the large size of the unit cell.

In the DFT/MD calculations the number of water molecules in the interlayer region was varied from two to eight in the presence of one carbon dioxide molecule. The system was first equilibrated using the isobaric-isothermal ensemble (NPT) with T = 348.15 K and P = 130 bar, conditions close to those existing in subsurface geological reservoirs and caprocks, and also to those used in CO_2 intercalation experiments in clays carried out at National Energy Technology Laboratory (NETL) (Romanov, 2013). Starting from initial structures relaxed using MD simulations with force fields (see Section 2.2), an equilibration time of 15 picosecond (ps) was employed, followed by 20 ps production runs using the microcanonical ensemble. The velocity Verlet algorithm was then used to update positions every 0.5 femtosecond (fs). To reduce the energy drift to 1 K/ps, the energy convergence tolerance for the electronic self-consistency cycle at each Born-Oppenheimer step was set to 10^{-6} eV. The atomic velocities were collected every 2

fs for up to 20 ps from production runs and used to calculate the velocity autocorrelation functions (VACF) (Allen and Tildesley, 1987), which, in turn, were used to calculate the power spectra. The velocity autocorrelation function for CO_2 was computed using the standard definition:

$$C(t) = \frac{1}{3N}\sum_i^{3N} v_i(0) \cdot v_i(t) \quad (1)$$

where $v_i(t)$ is the velocity of the i-th CO_2 atom at time t, and N is the number of molecules in the simulation.

2.2 MOLECULAR DYNAMICS SIMULATIONS USING FORCE FIELDS

The force field calculations were carried out using the GROMACS package (van der Spoel et al., 2013). For the clay system, the Clayff force field (Cygan et al., 2004) which consists of non-bonded (electrostatic and van der Waals) terms parameterized for use with layered minerals was used. In Clayff the pairwise energy between atoms i and j separated by a distance r_{ij} is given by:

$$E_{ij} = \frac{q_i q_j e^2}{4\pi\epsilon_0 r_{ij}} + 4\varepsilon_{ij}\left[\left(\frac{\sigma_{ij}}{r_{ij}}\right)^{12} - \left(\frac{\sigma_{ij}}{r_{ij}}\right)^{6}\right] \quad (2)$$

where q_i is the charge on atom i, e is the elementary charge of an electron, ϵ_0 is the vacuum permittivity, and ε_{ij} and σ_{ij} are the Lennard-Jones energy and distance parameters, respectively. The flexible SPC (Berendsen et al., 1981) model was engaged for the water molecules placed in the interlayer space and for the layer hydroxyl groups. For CO_2, a recently developed flexible potential including intramolecular bond stretch and angle bend was used (Cygan et al., 2012). The general expression for the total potential energy is:

$$E_{\text{Total}} = E_{\text{Coul}} + E_{\text{VDW}} + E_{\text{Stretch}} + E_{\text{Bend}}, \quad (3)$$

where harmonic potentials are used for the bond stretch and angle bend terms:

$$E_{\text{Stretch}} = \frac{1}{2}k_{\text{S}}\left(r_{ij} - r_o\right)^2 \quad (4)$$

and

$$E_{\text{Bend}} = \frac{1}{2}k_{\text{B}}\left(\theta_{ijk} - \theta_o\right)^2 \quad (5)$$

The optimized force field parameters for CO_2, presented in Table 1, were combined with those in Clayff (Cygan et al., 2004) to model CO_2 intercalation into hydrated MMT. The Lorentz-Berthelot mixing rule (Allen and Tildesley, 1987) was used to obtain the Lennard-Jones (LJ) parameters for interactions between unlike atoms. The simulations were performed under periodic boundary conditions, with the long-range electrostatics treated by the particle-particle particle-mesh (PPPM) Ewald method (Allen and Tildesley, 1987). The cut-off radii for the non-bonded van der Waals interactions and for the Ewald summation of the electrostatics were chosen to be 12 Å, with switching distances starting from 11 Å. Due to the use of cut-offs for the LJ interactions, long-range dispersion corrections for energy and pressure were applied (van der Spoel et al., 2013). The leap-frog algorithm (van Gunsteren and Berendsen, 1988) was used to update positions every 1 fs.

Table 1: Force field parameters for CO_2

Non-bonding		Bonding	
q_C	+0.6512 e	k_{CO}	8443 kJ/mol Å^2
q_O	-0.3256 e	$r_{o\,CO}$	1.162 Å
ε_C	0.2340 kJ/mol	k_{OCO}	451.9 kJ/mol rad^2
ε_O	0.6683 kJ/mol	$\theta_{o\,OCO}$	180.0°
σ_C	2.800 Å		
σ_O	3.028 Å		

The general chemical formula used for the sodium montmorillonite is $Na_xMg_xAl_{2-x}Si_4O_{10}(OH)_2{\cdot}nH_2O$, where the layer charge resides on the octahedral sheet (tetrahedral substitutions such as Al^{3+} for Si^{4+} can also occur but are not considered here). For the molecular dynamics simulations with the Clayff force field (Cygan et al., 2004), the MMT structural model was created by replicating a pyrophyllite unit cell with an isomorphic octahedral Al^{3+}/Mg^{2+} substitution to produce a triclinic 8 x 4 x 4 supercell (64 times larger than the supercell used for the DFT-based MD simulations). The negative charge introduced by the substitution is compensated by 96 sodium ions residing in the interlayers. The stoichiometry is $Na_{0.75}Mg_{0.75}Al_{3.25}(OH)_4(Si_4O_{10})_2$ with a layer charge of 0.75 per $O_{20}(OH)_4$ layer unit. This results in 5,120 atoms constituting the clay phase. The CO_2 content was varied from 0.5 to 4 molecules per unit cell and the water content was varied from one to nine molecules per unit cell. The H_2O/CO_2 composition in the interlayer region is designated as *X*-*Y*, where *X* and *Y* are, respectively, the numbers of water and CO_2 molecules per unit cell. Particular emphasis is placed on scenarios with three and five water molecules per unit cell. The former composition provides a partially saturated water monolayer (with $d \sim 11.4$ Å), which is close to that of the samples used to study the impact of CO_2 exposure to Na-MMT in high pressure experiments (Giesting et al., 2012; Schaef et al., 2012). The latter composition gives a *d*-spacing of 12.2 Å, which corresponds to a fully saturated monolayer (1W).[4] In the 1 W state MMT structure demonstrates a sharp decrease in ability to capture dry CO_2 as reported in high-pressure X-ray diffraction experiments (Giesting et al., 2012; Schaef et al., 2012). Relaxation of MMT with intercalated species was performed using the *NPT* ensemble at $T = 348.15$K and $P = 130$ bar as well as at $T =$ 300 K and $P = 1$ bar to study the dependence of the basal spacing on pressure. Equilibration runs of 1 ns were carried out followed by 20 ns production runs in the *NPT* ensemble, with *semi-isotropic* pressure coupling permitting the *z*-dimension to fluctuate independently from the *x* and *y* directions. Pressure was controlled by a Parrinello-Rahman barostat (Parrinello and Rahman, 1981; Nóse and Klein, 1983) with a relaxation time of 4 ps, and temperature was controlled by a Nóse-Hoover thermostat (Nóse, 1984; Hoover, 1985) with a relaxation time of 2 ps. A time step of 1 fs was used in the simulations.

The radial distribution function (RDF) for species *B* around *A* is calculated as:

$$G_{A-B}(r) = \frac{1}{4\pi\rho_B r^2}\frac{dN_{A-B}}{dr} \tag{6}$$

where ρ_B is the number density of species B, and dN_{A-B} is the average number of type *B* particles lying in the region *r* to *r*+*dr* from a type A particle. N_{A-B} is the coordination number for *B* around *A*.

To calculate the diffusion coefficients of the interlayer species, the Einstein relation was employed using equilibrated atomic trajectories from the *NVT* ensemble simulations with 1 ps sampling to evaluate the mean square displacement of the molecules and ions:

$$D = \lim_{t\to\infty}\frac{1}{6N_m t}\sum_{j=1}^{N_m}\left[r_j(t) - r_j(0)\right]^2 \tag{7}$$

where N_m is a number of a selected species and $r_i(t)$ is the center-of-mass position of the i^{th} species at time t. The averages were over 4 ns trajectories. The diffusion coefficients were derived from the linear slope of the mean square displacement as a function of the simulation time. Different restart points in the analysis were taken to monitor convergence.

3. EXPERIMENTAL DETAILS

Diffuse Reflectance Infrared Fourier-Transform Spectroscopy (DRIFTS)

The clay samples used in this work were powders of SWy-2 (natural Na-rich-MMT from Wyoming) and STx-1b (natural Ca-rich-MMT from Texas) acquired from the Source Clays Repository (Costanzo, 2001; Martin, 1979). An FT-IR spectrometer (Thermo Electron Corporation, Model Nicolet 8700) with a Smart Collector and dual environmental chamber was used to obtain diffuse reflectance infrared spectra. The spectra were collected in a nitrogen flow-through environment, after 8 hrs of exposure of the clay samples to 1,500 psig (~10 MPa) pressure of CO_2 at 55°C. In each measurement, 100 scans were completed with 4 cm^{-1} resolution. KBr diffuse reflectance spectra were used as a background reference. More details on the experimental setup and execution can be found in Romanov (2013) and other studies.

4. ANALYSIS OF D-SPACING, RADIAL DISTRIBUTION FUNCTIONS, AND DENSITY PROFILES FOR CARBON DIOXIDE-WATER-SODIUM-MONTMORILLONITE SYSTEMS

Figure 1 shows a schematic representation of the montmorillonite TOT layers and interlayer species (H_2O, CO_2, Na^+) considered in this study. Figure 2 reports the expansion of the *d*-spacing of Na-MMT upon intercalation of water computed using MD simulations with the Clayff force field (Cygan et al., 2004). Comparison with experimental data shows that the MD results closely reproduce the experimental trend in the *d*-spacing, displaying plateaus corresponding to formation of monolayer and bilayer water in the interlayer. It is important to note that it is a generally accepted paradigm among clay mineralogists that coexistence of different hydration states (0W, 1W, 2W) in a smectite sample is common even under controlled conditions (Ferrage et al., 2005). It is also generally accepted that fractional hydration states correspond to a sample with different integer hydration structures. For example, the diffuse character of the (00l) reflections, at the transition between two discrete hydration states, and the asymmetric (001) peak profile provides evidence that the MMT structure evolves gradually from one hydration state to the other through mixed-layer structures composed of discrete hydration states (Sato et al., 1992; Ferrage et al., 2007). Therefore, the experimental data outside of the ranges designated by the dotted lines in Figure 2 may have originated from a mixture of montmorillonite at different hydration states. In the simulations the structures corresponding to the intermediate *d*-spacing values were obtained from well-defined model systems with controlled amounts of water in the interlayer. Hydration levels intermediate between 0W and 1W and intermediate between 1W and 2W provide equilibrated structures with parallel TOT clay layers as necessary to obtain a series of basal diffraction peaks. Thus, these calculations suggest that smectite minerals could exist at fractional hydration states. However, it is possible that these are obscured in experimental diffraction studies by the mixed hydration states.

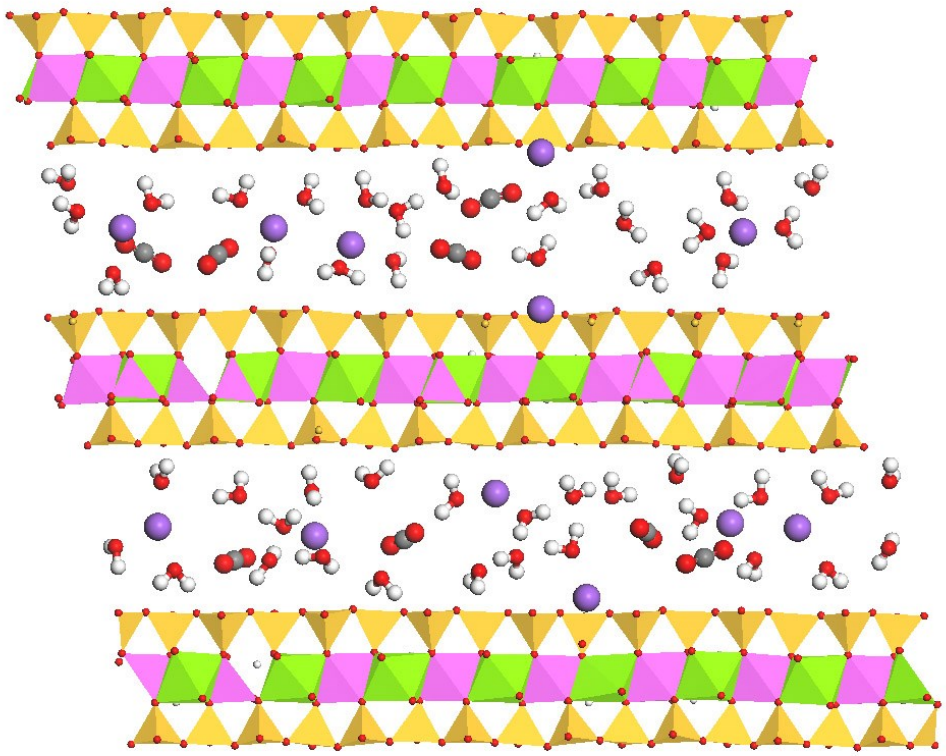

Figure 1: Schematic representation of the clay/H_2O/CO_2 system. Color designation: red balls – oxygens, purple – sodium ions, white – hydrogens, and grey – carbon.

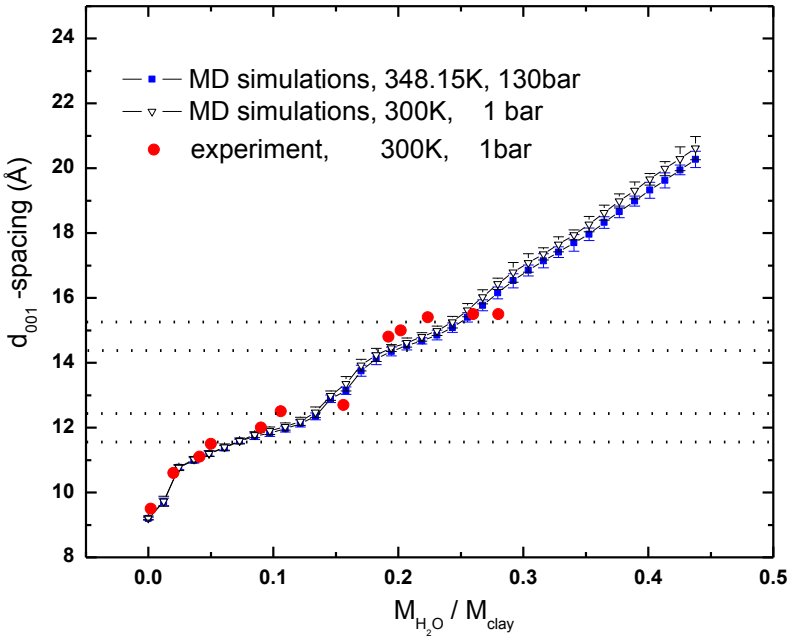

Figure 2: Swelling behavior of sodium-montmorillonite clay upon hydration. Comparison of calculated and experiment results (red circles) from Fu et al. (1990). Dotted lines indicate ranges of basal *d*-spacing corresponding to the 1W and 2W hydration states.

The spacing calculated for the *P*-*T* conditions employed in the NETL experiment (*T* = 75 °C and *P* = 130 bar) (Romanov, 2013) deviates only slightly from that calculated at *P* = 1 bar and lower temperature. Thus, the *d*-spacing is relatively insensitive to changes in pressure and temperature, with the degree of water content being the main factor controlling the extent of swelling. This is consistent with XRD-measurements of *d*-spacings showing that hydrate states are relatively stable with pressure (Fu et al., 1990; Giesting et al., 2012; Ilton et al., 2012).

DFT calculations have shown that the adsorption of dry CO_2 in the interlamellar space of non-hydrated Na-MMT is energetically unfavorable (Voora, 2013). This is consistent with results of Gibbs ensemble Monte Carlo simulations using classical force fields that revealed that dry CO_2 in Na-MMT is unstable except at large (>2W) *d*-spacing values (Yu and Yang, 2011). In order to study CO_2 intercalation, force field MD simulations with the water content varied from 1–9 H_2O molecules per unit cell were performed. Figure 3 displays the calculated interlayer distance as a function of the number of water molecules for selected numbers of intercalated carbon dioxide molecules per unit cell. The bottom curve, which reports the results in the absence of intercalated CO_2 molecules, serves as the reference. As seen in Figure 3, intercalation of CO_2 causes an expansion of the interlamellar spacing comparable to that caused by increasing hydration. Full monolayer coverage is achieved for 5 H_2O molecules per unit cell, as well as for $4H_2O+1CO_2$, $2H_2O+2CO_2$, or $1H_2O+3CO_2$. In the latter two cases, the fact that $nH_2O+mCO_2 = 4$ rather than 5 reflects the larger size of the CO_2 molecule compared to H_2O. Similarly, full bilayer coverage can be achieved with compositions ranging from 9 H_2O molecules to 3 H_2O molecules with 3 CO_2 molecules. At a water content of 6 molecules per unit cell, the addition of a single CO_2

molecule per unit cell results in expansion of the *d*-spacing to a value close to that of the 2W state. However, the latter process appears to be thermodynamically unfavorable as intercalation of CO_2 was not observed in several in-situ XRD studies (Giesting et al., 2012; Schaef et al., 2012; Ilton et al., 2012) on Na- and Ca-MMT with the initial *d*-spacing corresponding to the fully saturated 1W state (i.e., 5–6 H_2O molecules per unit cell). At *d*-spacing distances of ~14–15 Å (corresponding to the 2W state) a distinct plateau is observed for fixed CO_2 concentrations over a range of initial water content (Figure 3). For example, 8–0.5, 7–1, and 6–2 water-CO_2 compositions all have similar *d*-spacings. As a result, in the 2W hydration state CO_2 incorporation can displace water keeping the *d*-spacing nearly constant rather than further expanding the interlayer spacing.

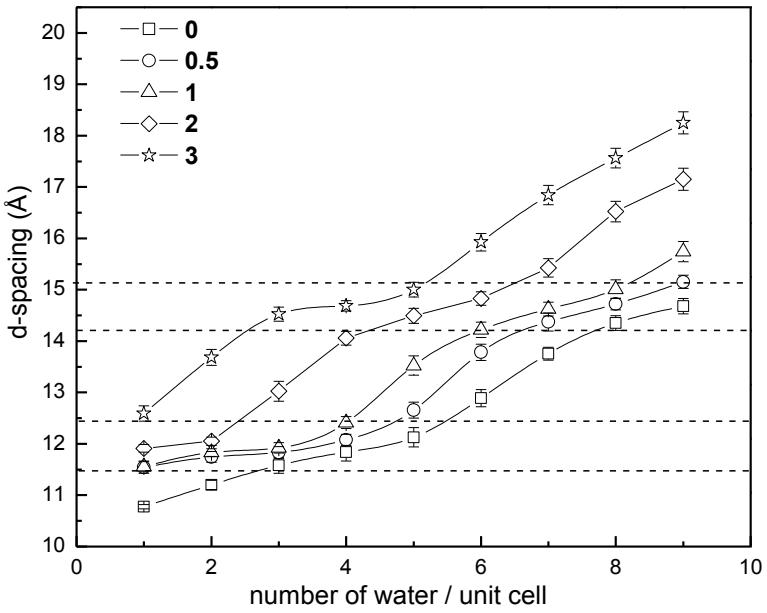

Figure 3: *d*-spacing as a function of number of water molecules at fixed numbers of CO_2 molecules per unit cell. Dashed lines indicate ranges of basal *d*-spacing corresponding to 1W and 2W hydration states.

To explore the distribution of the various species in the interlamellar space of the clay, density profiles were calculated for 3-Y and 5-Y compositions. Figures 4 and 5 display the resulting density profiles computed along the *z* axis (perpendicular to the clay surface) and averaged over the interlayer region of the simulation box. The amounts of CO_2 were chosen to induce *d*-spacing expansion toward the 1W, 2W, and 3W hydration states. The distributions confirm that H_2O and CO_2 molecules indeed form well-defined layered structures similar to pure 1W and 2W hydration states. Figure 4a reports the profiles for the 1W state, which, upon addition of one more CO_2 molecule per cell, starts to form the 2W state (Figure 4b). Figure 4b reports the profiles for a "non-saturated" 2W system, while Figure 5b represents a fully saturated 2W. Figures 4c and 5c report the density profiles at the interlayer distances corresponding to the 3W

hydration state. At those spacings (3W) the simulations show that the center layer is composed almost entirely of CO_2 molecules sandwiched between two layers of the CO_2/H_2O mixture.

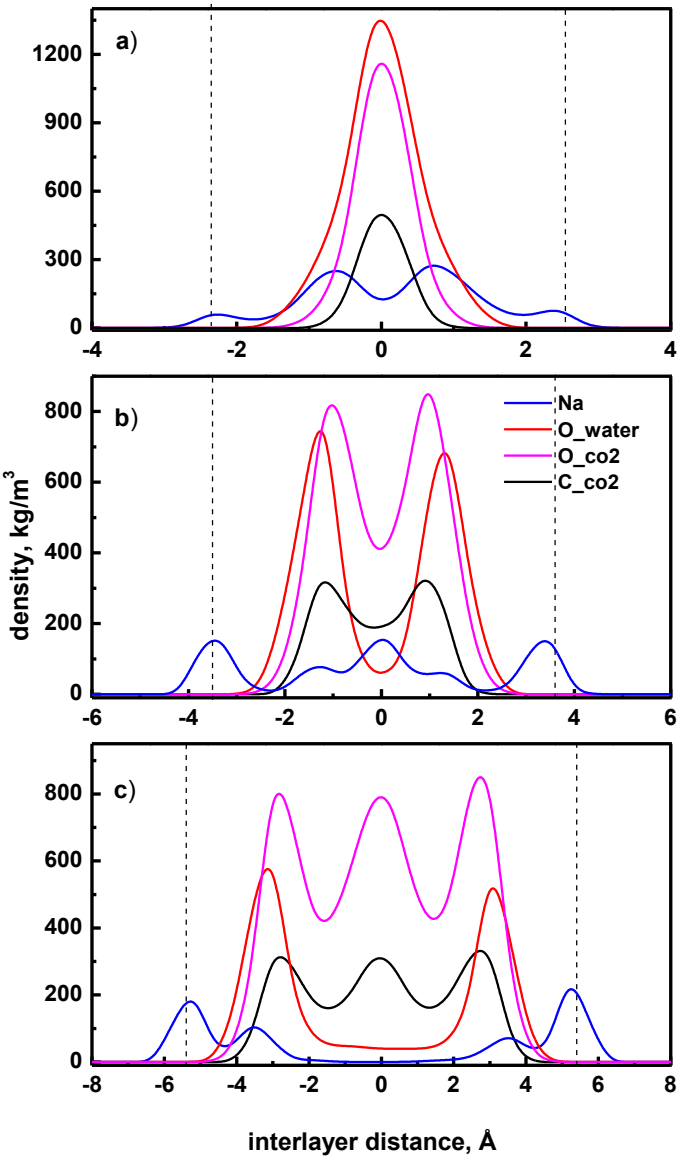

Figure 4: Density profiles along the interlayer distance perpendicular to the internal surfaces of Na-MMT showing distribution of the intercalated species for a) 3-1, b) 3-2, and c) 3-4 compositions. Dashed lines designate the planes of basal oxygens.

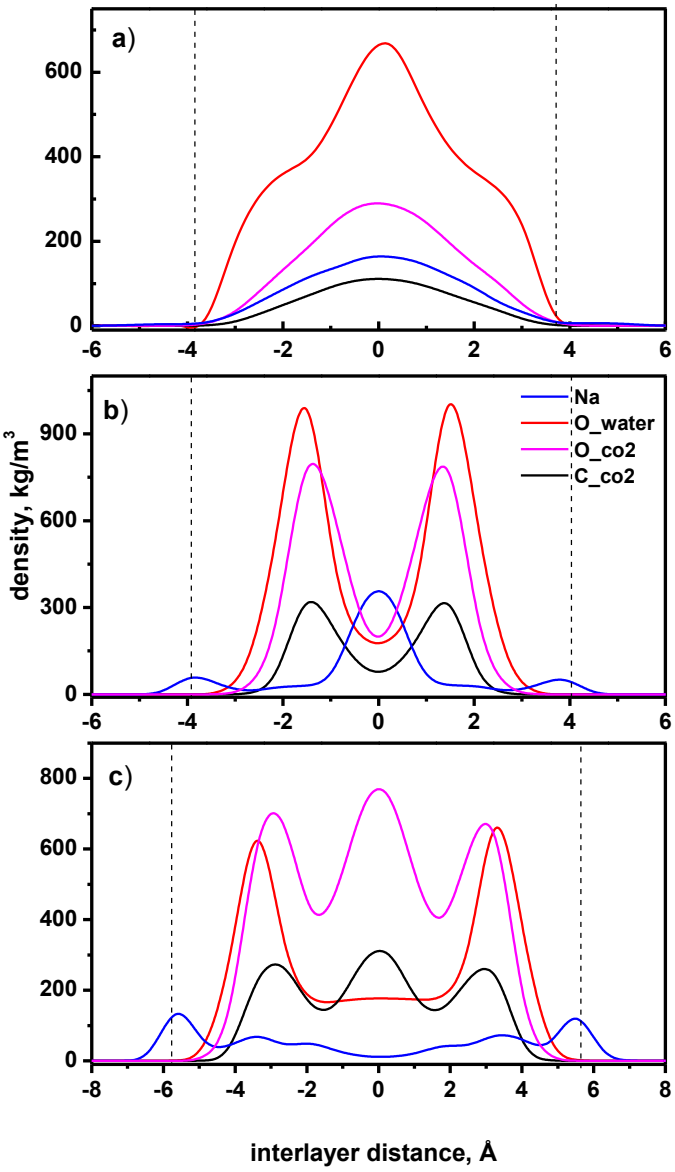

Figure 5: Density profiles along the interlayer distance perpendicular to the internal surfaces of Na-MMT showing distribution of the intercalated species for a) 5-1, b) 5-2, and c) 5-4 compositions. Dashed lines designate the planes of basal oxygens.

The ability of water molecules to induce swelling in a stepwise fashion is related to the formation of an extended hydrogen bonding network and interaction of the water molecules with clay surface (Fu et al., 1990). The carbon dioxide can be expected to participate in interaction with water and clay surfaces. In this regard, it is instructive to consider the orientational behavior of CO_2 in the confining environment of MMT. This is accomplished by examining the distribution of angles between the CO_2 axial orientation and the axis perpendicular to the clay surfaces. Figure 6 reports this distribution computed for each CO_2 molecule using the C-O bond most nearly perpendicular to the surface at H_2O/CO_2 compositions corresponding to 1W, 2W, and 3W hydration states. At each state a normal distribution centered around 90° is obtained indicating that the carbon dioxide molecules are preferentially oriented parallel to the confining clay surfaces. With increasing number of water-CO_2 layers, the CO_2 molecules explore a wider range of angles consistent with greater rotational freedom in the interlayer. Inspection of the corresponding MD trajectories reveals that the CO_2 molecules display no specific coordination to the atoms comprising MMT. These data are consistent with experimental observations that MMT has to be wetted in order to intercalate CO_2 (Giesting et al., 2012; Schaef et al., 2012; Ilton et al., 2012). Thus, the compositions providing the density profiles depicted in Figures 4c and 5c with a central CO_2 layer are likely to be unstable with respect to collapse to a more stable bilayer form (Figures 4b, 5b) by expelling CO_2 molecules or to expansion into the 3W hydration state by incorporating more water molecules.

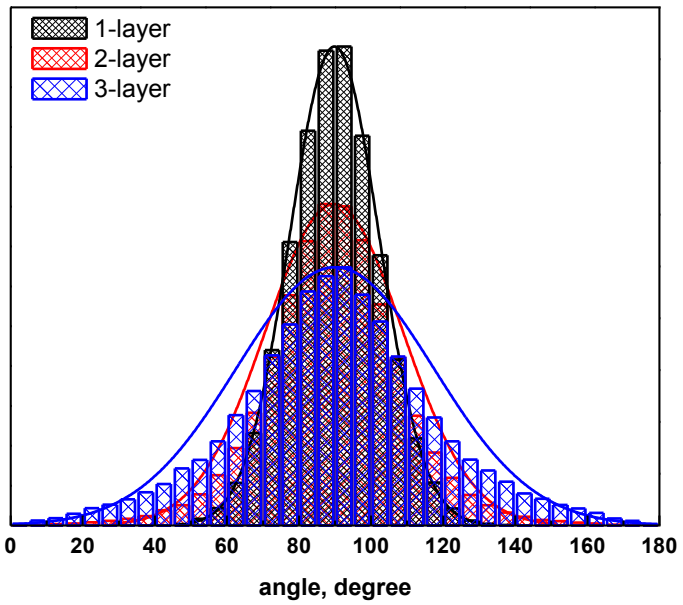

Figure 6: Histograms of angular distribution for CO_2 orientation relative to the axis perpendicular to clay surface. Data averaged over 30 CO_2 molecules for every composition during 4 ns.

As seen in Figures 4 and 5, pronounced changes occur in the density profiles of the Na^+ ions with increasing CO_2 content. Specifically, the incorporation of CO_2 molecules into the interlayer region enhances the probability of finding Na^+ ions near the surfaces, thus splitting the Na^+ profiles into several peaks. The surface-bound sodium ions (inner-sphere adsorption) are coordinated above the centers of the hexagonal rings of silicon tetrahedra linked by shared basal oxygens. However, these ions retain strong interactions with nearby water molecules. In this regard, the amount of water should be an important factor determining the degree of ion adsorption. Indeed, comparison of Figures 4 and 5 shows that cation adsorption at the surface is less important in the systems having five water molecules per unit cell than in the systems with only three water molecules per unit cell. To quantify the adsorption process the concentrations of the Na^+ ions at the surfaces were calculated as a function of the carbon dioxide concentration. Figure 7 displays occupancy values of Na^+ ions near the centers of the hexagonal rings as a percentage of a total number of the rings for the 3-Y and 5-Y compositions.

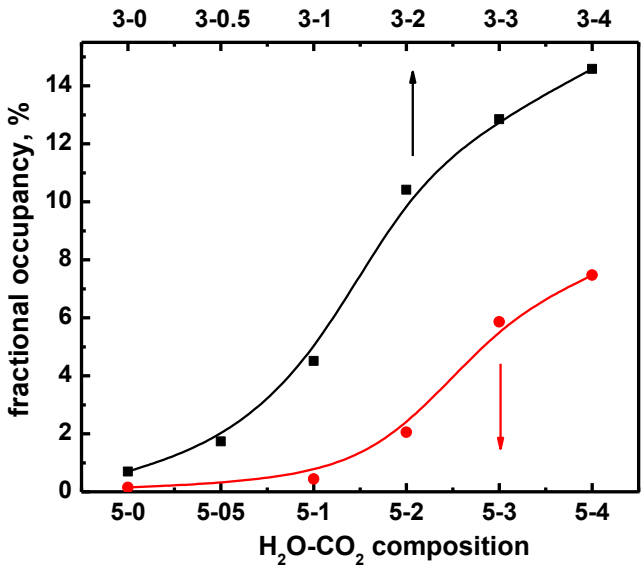

Figure 7: Fractional occupancy of the hexagonal sites on the internal clay surfaces by Na^+ as a function of H_2O/CO_2 composition in the interlayer.

To calculate these values the sodium atoms were counted as being adsorbed at the hexagonal rings when the ions had a residence time at the surface greater than 50% of the total simulation time. A Na+ ion was considered adsorbed at the surface if three and more distances between the sodium ion and basal oxygens become less than 2.9 Å. The adsorption of Na^+ ions on the internal surfaces depends strongly on the water content, with the extent of surface adsorption being greater for the 3-Y than for 5-Y composition. The 3-Y and 5-Y composition plots are reminiscent of a typical adsorption isotherm showing increase of Na^+ adsorbate concentration with increase of CO_2 content in the interlayer. The plot for the 5-Y composition reveals a more smooth behavior, with the preference for Na^+ to stay solvated in the interlayer in the absence of CO_2 content. Increasing the carbon dioxide concentration promotes migration of the ions to the clay

surfaces where they form inner-sphere surface complexes (Bourg and Sposito, 2011). The adsorption of sodium ions at the clay surfaces increases the hydrophobicity of the surfaces since the ions effectively shield the basal oxygens from hydrogen bonding with water molecules. This process could also be responsible for observed dewetting and increased contact angles on mica and silica surfaces during $scCO_2$ invasion under high ionic strength of brine (Wan et al., 2011).

In order to characterize how the various interactions impact the hydrogen bonding, hydrogen-bond lifetimes were computed following the approach described in van der Spoel et al. (2006). Table 2 reports the calculated hydrogen-bond lifetimes for water-clay, water-water, and water-carbon dioxide pairs at different carbon dioxide concentrations and two levels of water content. In general, the longest lived hydrogen bonds are those between water molecules followed by water-clay and then water-CO_2. This is consistent with the results of our recent investigation of water loading on the pyrophyllite surface that displayed stronger water-water than water-surface interactions (Zhang et al., 2012). Increased intercalation of carbon dioxide is accompanied by decreased H-bond lifetimes for all three types of interactions. This indicates that as the interlayer space is expanded, the molecular coordination becomes less structured (Table 2, Figure 6). Thus, expansion of the confining space to accommodate more CO_2 molecules translates into a more orientationally disordered arrangement of the interlayer water and carbon dioxide molecules.

Table 2: Calculated hydrogen bond lifetimes (τ, ps)[a]

Composition (X-Y)						
	3-0 (1L)	3-0.5 (1L)	3-1 (1L)	3-2 (2L)	3-3 (2L)	3-4 (3L)
$\tau_{H2O-H2O}$	7.36	9.31	15.28	12.21	6.28	5.92
$\tau_{H2O-CO2}$	-	6.48	8.65	2.77	2.64	1.71
$\tau_{H2O-clay}$	20.25	12.98	13.54	6.25	4.21	3.69
	5-0 (1L)		5-1 (1L)	5-2 (2L)	5-3 (3L)	5-4 (3L)
$\tau_{H2O-H2O}$	11.76		9.97	5.88	8.36	5.24
$\tau_{H2O-CO2}$	-		2.4	0.68	1.84	0.31
$\tau_{H2O-clay}$	5.15		7.22	2.17	4.57	1.43

[a] Number of layers is indicated in parenthesis.

5. CALCULATION OF DIFFUSION COEFFICIENTS FOR INTERLAYER SPECIES IN SODIUM MONTMORILLONITE

Table 3 reports the diffusion coefficients for interlayer species computed in this work as well as those obtained from experimental measurements in similar systems. The calculated values are reported for both diffusion in three-dimensional (3-D) space and for diffusion parallel to the clay surfaces. In the confining environment of nano-channels the lateral diffusion coefficients are more relevant. The data reported in Table 3 show that for both water and carbon dioxide molecules the diffusivities for lateral motion are about 30% greater than those for 3-D motion. Moreover, the diffusion coefficients of both CO_2 and H_2O increase with increasing concentration of CO_2 due to the associated expansion of the interlayer space. The diffusion coefficients of water computed for the systems without CO_2 (3-0 and 5-0) are in close agreement with the experimental values for interlayer water in MMT obtained using QENS spectroscopy (Marry et al., 2008) and neutron spin echo for synthetic Na-hectorite (Marry et al., 2011), a trioctahedral smectite with isomorphous substitution in the octahedral sheet that displays the similar swelling properties as MMT and has comparable diffusion coefficients (Malikova et al., 2007). The diffusion coefficients of H_2O and CO_2 in the interlayer of Na-MMT calculated for the 3-1 composition are in agreement with those computed by Botan et al. (2010) for a similar composition. Formation of the second and third water/CO_2 layers induced by CO_2 intercalation leads to stepwise increases in diffusivity of carbon dioxide compared to the values obtained for the monolayer arrangement. The effect of clay swelling on the diffusion coefficients is more pronounced for CO_2 than for water. For example, for the 3-Y composition the change from mono- to the bilayer arrangement is accompanied by nearly an order of magnitude increase of the CO_2 diffusion coefficients, while the corresponding change for water is only about a factor of two (Table 3). The greater impact of the interlayer spacing on the CO_2 diffusivity can be understood in terms of the preferred parallel orientation of the CO_2 molecules relative to the clay surface.

Table 3: Diffusion coefficients ($\times 10^{-5}$ cm^2/s) of water, carbon dioxide molecules, and Na^+ cations[a] in the interlayer space of sodium montmorillonite.

Composition X-Y						
Diffusion coef.	3-0 (1L)	3-0.5 (1L)	3-1 (1L)	3-2 (2L)	3-3 (2L)	3-4 (3L)
D^{H2O}	0.26±0.02	0.26±0.02	0.14± 0.02	0.24±0.05	0.35± 0.03	0.68±0.07
D_{xy}^{H2O}	0.39± 0.03 0.28[b]; 1.0± 0.1[c]	0.39± 0.02	0.21± 0.02 0.32(2)[c]	0.36± 0.04	0.52± 0.07	1.01±0.09
	5-0 (1L)		5-1 (2L)	5-2 (2L)	5-3 (3L)	5-4 (3L)
D^{H2O}	0.21±0.02		0.47±0.06	0.53±0.02	0.52±0.01	0.72±0.06
D_{xy}^{H2O}	0.30±0.02 0.28[b]; 1.0± 0.1[c]		0.70±0.08	0.80±0.03	0.80±0.06	1.08±0.08
	3-0 (1L)	3-0.5 (1L)	3-1 (1L)	3-2 (2L)	3-3 (2L)	3-4 (3L)
D^{CO2}		0.16± 0.01	0.12± 0.01	0.92± 0.05	1.10± 0.07	2.23±0.15
D_{xy}^{CO2}		0.23± 0.01	0.18± 0.01 0.17(2)[d]	1.38± 0.08	1.65± 0.08	3.12±0.17
	5-0 (1L)		5-1 (2L)	5-2 (2L)	5-3 (3L)	5-4 (3L)
D^{CO2}			0.55±0.05	0.77±0.07	1.49±0.25	2.82±0.13
D_{xy}^{CO2}			0.82±0.05	1.15±0.11	2.24±0.34	4.23±0.17
	3-0 (1L)	3-0.5 (1L)	3-1 (1L)	3-2 (2L)	3-3 (2L)	3-4 (3L)
D^{Na+}	0.04±0.01	0.08±0.01	0.07±0.01	0.05±0.01	0.06±0.01 *0.25±0.17*	0.10±0.02 *0.48±0.22*
D_{xy}^{Na+}	0.06±0.02	0.12±0.01	0.10±0.02 0.13(2)[d]	0.08±0.02	0.08±0.01 *0.37±0.26*	0.12±0.03 *0.58±0.31*
	5-0 (1L)		5-1 (2L)	5-2 (2L)	5-3 (3L)	5-4 (3L)
D^{Na+}	0.12±0.01		0.17±0.04	0.21±0.01	0.13±0.03 *0.21±0.09*	0.10±0.01 *0.26±0.14*
D_{xy}^{Na+}	0.17±0.02		0.24±0.04	0.31±0.01	0.19±0.04 *0.32±0.12*	0.14±0.01 *0.39±0.11*

[a] The italic font is used to designate coefficients calculated for sodium cations solvated by water in the interlayer space. D_{xy} denotes lateral diffusion coefficients for motion parallel to clay surfaces. Number of layers is given after a composition notation in the parenthesis.

[b] Marry et al., 2008

[c] Marry et al., 2011

[d] Botan et al., 2010

At basal *d*-spacings corresponding to three layers (where the central layer comprised solely of CO_2 molecules is sandwiched by two CO_2/water layers), the lateral diffusion coefficient for CO_2 attains a value of $4.23\pm0.17\times10^{-5}$ cm^2/s. This value comprises contributions from both the CO_2 in water layers and the central CO_2 layer, and is comparable to that measured for diffusion of CO_2 in bulk water at $5.40\pm0.10\times10^{-5}$ cm^2/s (T = 348.15 K) (Lindeberg and Wessel-Berg, 1997). Expansion of the interlayer space due to an increase of the carbon dioxide content and subsequent formation of multilayers formed by interlayer species leads to an increase in diffusion coefficients of water (Table 3). The calculated diffusion constants of H_2O in MMT are in good agreement with measured diffusion constants for water in clay interlayer spaces. The measured diffusion coefficient of water in the bulk at T = 343 K is 5.65×10^{-5} cm^2/s (Thomas and Adams, 1965) which is more than an order of magnitude greater than that for water confined between clay layers.

In the case of Na^+ ions, direct comparison of the computed and experimental values of the diffusion constants can be misleading since measured ionic mobilities in montmorillonite samples can have contributions from pores and external surfaces as well as from the interlayer spaces depending on experimental conditions and ionic strength (Kozaki et al., 1998, 2008). Kozaki et al. (1998, 2008) reported a diffusion constant of 1.8×10^{-6} cm^2/s for interlayer sodium ions in the 2W hydration state of MMT at T = 323 K and 0.1-0.3 M concentrations. This value is close to the computed diffusion constants of sodium ions in the interlayer space (Table 3). The intercalation of CO_2 has only a moderate effect on the diffusion coefficient of the sodium ions. However, the computed diffusion constants include contributions from the surface-adsorbed ions which grow in importance as the CO_2 content increases (Figures 4 and 5). Calculations were also carried out where diffusion of the interior sodium ions was separated from contributions from surface-bound Na^+ ions. Not surprisingly, the diffusion coefficients for non-surface bound Na^+ ions are much larger than those computed for total Na^+ ions for compositions with high CO_2 content (Table 3). Such behavior is attributed to increased adsorption of Na^+ at the surface as CO_2 concentration increases (Figure 7).

6. INTERPRETATION OF INFRARED SPECTRA OF CO_2 TRAPPED IN SODIUM MONTMORILLONITE

CO_2 trapped in MMT produces a distinctive infrared reflectance spectrum (Romanov et al., 2010a,b; Romanov, 2013). Figure 8 compares the asymmetric stretching region of Fourier transform infrared spectra of gaseous CO_2 and of CO_2 trapped in Ca-MMT (STx-1b) and Na-MMT (SWy-2) clays. The gas-phase CO_2 molecule has rotational-vibrational adsorption bands even though it has a zero permanent dipole. This is a consequence of the asymmetric (ν_3) stretch and bending modes inducing oscillating dipole moments. The selection rule for the band involving excitation of ν_3 is $\Delta J = \pm 1$ corresponding to *P* and *R* branches (where J is the rotational quantum number). The *Q* branch with $\Delta J = 0$ is forbidden and deduced to occur at ~2,349 cm^{-1} (Figure 8, the vertical line). For CO_2 intercalated in a clay phase the selection rule that makes the Q-branch forbidden in the gas phase is lifted, and the spectra reveal a strong signal due to the CO_2 asymmetric stretch vibrational mode (Papousek and Aliev, 1982). Rotational states of adsorbed molecules are frustrated by orientation-dependent perturbations within the surface potential wells (Brown et al., 1999; Schaffert et al., 2013) and the ro-vibrational P, Q, R branches collapse into a broad vibrational band, which is characteristic of physisorption (Kono et al., 1983). The peak maximum is red-shifted by 5 cm^{-1} in Na-MMT and by 10 cm^{-1} in Ca-MMT relative to that of the fundamental of gaseous CO_2. These small frequency shifts indicate that carbon dioxide molecules are not engaged in strong interactions.

Classical molecular dynamics simulations were carried out to compute the power spectra of CO_2 intercalated in Na-MMT with $(H_2O)_n(CO_2)_m$, compositions of n=1-9 and m=1-4 per unit cell. These calculations provide a frequency of the CO_2 asymmetric stretch vibration essentially identical to that of the gas-phase molecule calculated using the same theoretical method. The failure of the classical MD simulations to predict a red shift of the CO_2 asymmetric stretch vibration is indicative of a deficiency in the force field. This led us to also calculate the power spectra using DFT-based MD simulations. Details of these calculations are given in Section 2.1 The supercell employed is comprised of two unit cells and contains one CO_2 molecule and two to eight water molecules in the interlayer region. The calculated power spectra are reported in Figure 9 from which it is seen that the calculated asymmetric stretch vibration of CO_2 is shifted 6 cm^{-1} to the blue in MMT1 and 11 cm^{-1} to the red in MMT4 compared to the corresponding gas-phase fundamental. For the systems incorporating intermediate numbers of water molecules the calculated value of the CO_2 asymmetric stretch frequency resides between these limits. This demonstrates that the hydration level strongly affects the direction and magnitude of the frequency shift. Inspection of the snapshots from the simulation trajectory of the MMT1 system reveals that the CO_2 molecule is primarily coordinated to a sodium cation due to an insufficient number of water molecules to efficiently hydrate the cations. The blue shift calculated for CO_2 interacting with a sodium cation is consistent with the experimental results for CO_2–cation complexes (Gregoire and Duncan, 2002; Walker et al. 2003; Jaeger et al., 2004). Increasing water content leads to formation of a hydration shell, release of CO_2 from coordination with the interlayer Na^+ ions, which, in turn, leads to a red shift of the asymmetric stretch vibration.

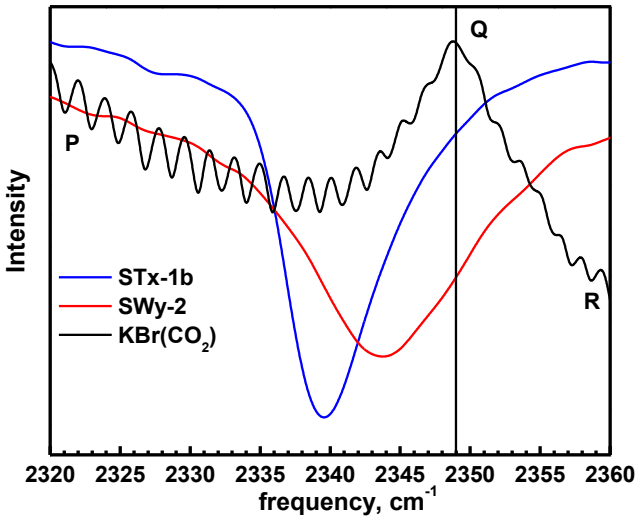

Figure 8: FT-IR diffuse-reflectance spectra of CO_2-treated smectite clay powders, Ca-MMT (STx-1b) and Na-MMT (SWy-2). KBr reflectance spectra were used for background subtraction. The vertical line marks the position of CO_2 asymmetric stretch fundamental (ν_3) for the gas phase; P, Q, and R branches represent the rovibrational coupling.

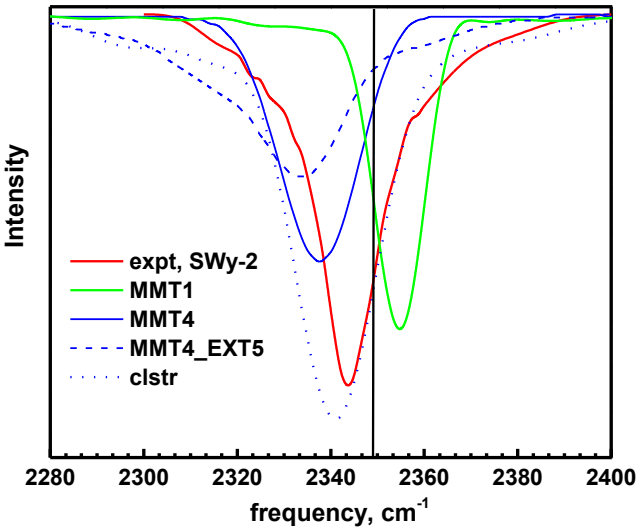

Figure 9: Comparison of the FT-IR asymmetric stretch mode for CO_2 intercalated into Na-MMT (expt, SWy-2) with the signal predicted using the power spectra for Na-MMT with 4 H_2O and 0.5 CO_2 molecules per unit cell (MMT4); with 1 water and 0.5 CO_2 molecules per unit cell (MMT1) with 4 water and 0.5 CO_2 molecules per unit cell with interlayer distance increased by 5 Å (MMT4_EXT5); and for a cluster of water and CO_2 molecules (clstr, see the text). The adjustment coefficient is 0.9941. The vertical line marks the CO_2 asymmetric stretch fundamental for the gas-phase.

To gain additional insight into the role of the CO_2-H_2O interactions, the O_w–C and $H_w - O_{CO_2}$ RDFs were calculated. Figures 10a and 10b report the RDFs for O_w–C and $H_w - O_{CO_2}$ pairs obtained from DFT-based and classical MD simulations at various H_2O/CO_2 compositions.

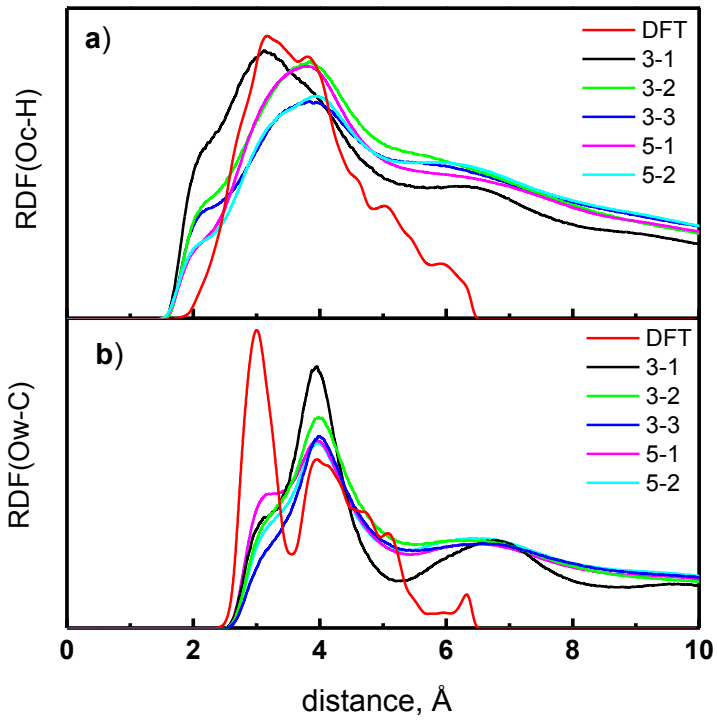

Figure 10: Oxygen (CO_2) –hydrogen (H_2O), and b) oxygen (H_2O)-carbon radial distribution functions for Na-MMT at various compositions of H_2O and CO_2. The RDFs designated as X-Y were obtained from classical MD simulations. The RDF marked as DFT was obtained from the DFT/MD simulations on the Na-MMT system with 4 H_2O and 0.5 CO_2 molecules per unit cell.

The $H_w - O_{CO_2}$ RDFs from the simulations using the force field display a shoulder near 2.3 Å, indicating formation of H-bonds between H_2O and CO_2. However, this shoulder recedes as the water content increases, and it is absent in the DFT-based MD simulations. Kumar et al. (2009), using Car-Parrinello MD simulations, obtained a similar $H_w - O_{CO_2}$ RDF consistent with little H-bonding between water and CO_2 molecules. The O_w-C RDF from the force field simulations give displays a weak shoulder near 3.1 Å, while that from DFT-based MD simulations has a pronounced peak around 2.9 Å which is close to the value reported for the global minimum of the CO_2-H_2O complex at the CCSD(T) level of theory (Garden et al., 2006; de Lange et al., 2011). These results indicate a possible shortcoming in the description of the CO_2-water interactions in the force field calculations. Recently, Vlcek et al. (2011) reported "polarization-corrected" LJ parameters for the unlike pair interactions in water/carbon dioxide mixtures, and used SPC/E and EPM2 force fields to simulate CO_2 in liquid water. The resulting RDFs closely

resemble those obtained from the classical force field simulations of CO_2 in hydrated MMT. Thus, the deficiency in the force field appears not to be related to the use of combination rules in determining the van der Waals parameters for CO_2 – water. It could reflect the inadequacy of a 3-point charge model for representing the electrostatic potential of CO_2.

In order to further explore the effect of the confining environment on the frequency of the CO_2 asymmetric stretch vibration, DFT-based MD simulations were also conducted on the MMT4 system with the basal distance extended by 5 Å. The extended interlayer space diminishes the effect of the basal oxygens and allows for a more flexible rearrangement of water molecules and interlayer ions during interaction with CO_2. For this system the asymmetric stretch vibration appears at 2,334 cm^{-1}, red-shifted by 15 cm^{-1} relative to the gas-phase value (Figure 9). This result provides further evidence of the pivotal role of the water molecules in the confining environment of clay in determining the frequency of the CO_2 asymmetric stretch fundamental. DFT-based MD simulations were also performed using a simulation box with a cluster of eight water molecules and one CO_2 molecule, and having dimensions corresponding to the interlayer space of the equilibrated MMT4 system. The frequency of the CO_2 asymmetric stretch is calculated to occur 8 cm^{-1} to the red from the fundamental vibration of the gas-phase CO_2 molecule (Figure 9). This is consistent with the peak in the experimental band of the asymmetric stretch showing a red shift about 6 cm^{-1} relative to the gas-phase molecule (Garrett-Roe et al., 2009; Moin et al., 2011).

To explore the origin of the red shift in the asymmetric stretch vibration of CO_2 intercalated in Na-MMT, snapshots were extracted from a DFT-based MD trajectory. The sampled structures show that the CO_2 molecule is surrounded by water molecules, many of which point OH groups toward the O atom of the CO_2 molecule. In several of the snapshots, the C-O bonds in the carbon dioxide molecule are slightly elongated in comparison with those of the gas-phase molecule (1.167 Å). Selected CO_2 molecules were then extracted and their vibrational frequencies were calculated at the B3LYP/aug-cc-pVDZ level of theory. As expected, the asymmetric stretch vibration is red-shifted in the distorted molecules compared to the equivalent vibrational mode of the optimized gas phase CO_2 molecule computed at the same level of theory. The frequency shift correlates in a linear manner with the extent of the distortion as seen from Figure 11. The insert 1 in Figure 11 reveals a histogram of the value summing the deviation of C-O bonds from the gas-phase value for MMT4 (Figure 9). The data shows that a normal distribution is centered around 0.02 Å indicating stretch of the bonds in interior space of montmorillonite. The similar trend is found for the neutral cluster of water and a carbon dioxide molecule (Insert 2, Figure 11). These results provide strong evidence that the observed red shift is primarily due to geometry distortions of the CO_2 molecule induced by the water molecules. In several cases with large CO bond length increases and large red shifts of the asymmetric stretch vibration, all H--O(CO_2) distances are greater than 4Å, strongly suggesting that it is electric field effects that are primarily responsible for the observed red shift. This also suggests that in the reported experiments (Loring et al., 2012; Romanov et al., 2010a,b; Romanov, 2013) hydration of CO_2 in the interlayer space is sufficient to form a solvation shell and preclude a direct interaction of CO_2 with sodium cations, which would act so as to cause a blue-shift (Gregoire and Duncan, 2002; Walker et al., 2003; Jaeger et al., 2004). Remarkably, a similar red shift in the stretch fundamental was found by Moin et al. (2011), in their mixed ab initio/force field MD simulations of carbon dioxide in water.

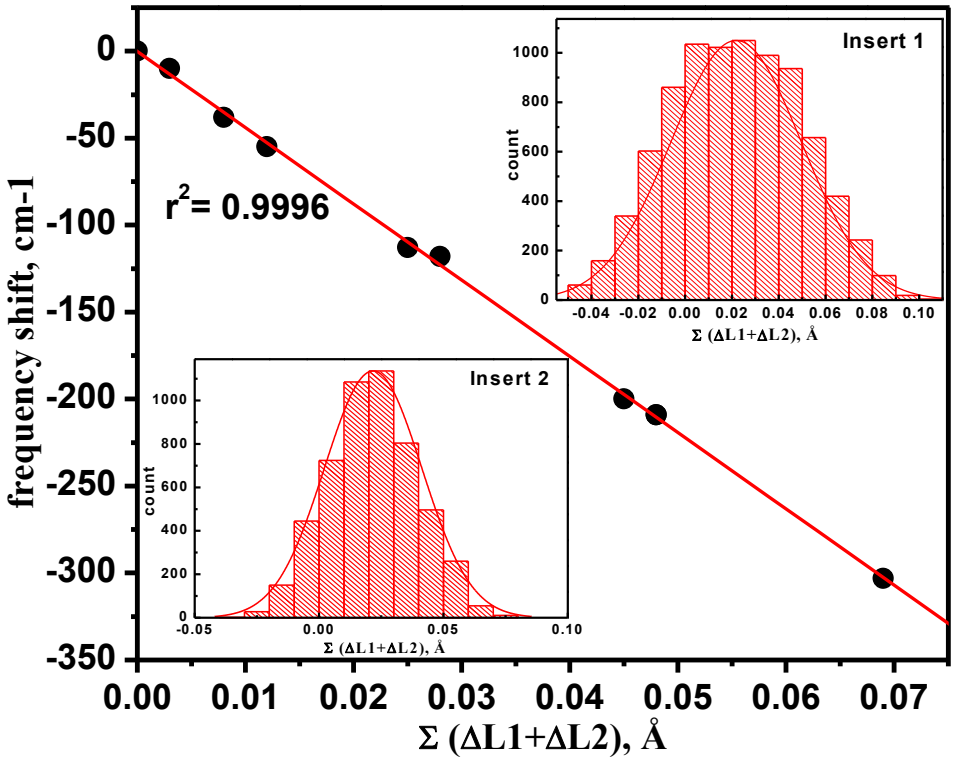

Figure 11: Correlation between a red shift of the asymmetric stretch vibration and a corresponding sum of incremental deviation of the bond lengths (ΔL1+ΔL2) for the CO_2 monomer relative to the gas-phase value. The insert 1 shows a histogram of geometry deviation values for CO_2 monomer in MMT4. The histogram data were obtained from a 15 ps DFT/MD trajectory. The insert 2 shows a histogram of geometry deviation values for CO_2 monomer in a cluster with eight water molecules in a simulation box (Figure 9 "clstr" and related text). The histogram data were obtained from a 10 ps DFT/MD trajectory.

These results explain why the classical MD simulations did not predict a red shift for the intercalated carbon dioxide. Specifically, the force field employed uses a harmonic C-O stretch term, whereas it is necessary to include an anharmonic C-O stretch term in the CO_2 force field to account for the frequency shift accompanying the stretch of the CO bonds upon hydration. This deficiency can be readily remedied, for example, by adopting a Morse-type potential to describe the C-O stretch potential.

7. CONCLUSION

One option for CO_2 storage is to use subsurface geological brine aquifers bound by low-permeability sealing caprocks. Caprock is often enriched with expandable clay minerals, and understanding the interaction between clay minerals, brines, and injected CO_2 is crucial for predictions of the natural seal integrity and site selection for long-term CO_2 storage. The integrity of the caprock is important because CO_2, being more buoyant than brine and oil, will tend to migrate above these relatively immiscible fluids.

Experimental measurements show that trapping of carbon dioxide in Na- and Ca-montmorillonite leads to a red shift in the asymmetric stretch frequency of the CO_2 molecule. DFT-based MD simulations were carried out to explain the origin of this red shift. The simulations reproduce the experimentally observed red shift and identify electric field induced elongation of the CO bonds of CO_2 as being primarily responsible for the frequency shift.

Force field molecular dynamics simulations were engaged to characterize in clay–water–CO_2 systems at pressure and temperature relevant to geological carbon sequestration. The simulations show that the degree of induced swelling caused by intercalation of CO_2 strongly depends on the initial water content in the interlayer space. Accumulation of CO_2 in the interlayer with humidity levels below those corresponding to the 1W hydration state first produces structures with basal *d*-spacings equivalent to 1W. Further carbon dioxide load promotes a stepwise expansion of the *d*-spacing to values equal to higher hydration states (2W and 3W). At water and CO_2 concentrations that give rise to mono- or bilayer arrangements in the interlayer region, the CO_2 molecules are preferentially oriented parallel to the clay surfaces. The hydrogen bond lifetimes are longest for H_2O-H_2O interactions followed by H_2O-O_{basal}, then by H_2O-CO_2. An important finding is that increasing the concentration of CO_2 promotes migration of the positively charged sodium ions to the clay basal surfaces. Sodium cations are found to absorb reversibly at the centers of hexagonal rings and form surface complexes that contribute to charge screening of the electrical layer and acting so as to increase the hydrophobicity of the surface. This process could be related to the increase of contact angle and dewetting on mica and silica surfaces during CO_2 invasion reported in series of experiments under conditions of high ionic strength of electrolyte (Wan et al., 2011). Thus, intercalation of CO_2 within smectite minerals in brine aquifers can cause significant changes in the clay phase *d*-spacing and modify wetting properties of the clay surfaces.

This page intentionally left blank

8. REFERENCES

Abdou, M. I.; Ahmaed, H. E. Evaluation of Low-solids Mud Reological Behavior during Drilling Shale Formation and Their Effect on the Pay Zone Productivity. *Petroleum Science and Technology* **2010,** *28*, 934–945.

Allen, M. P.; Tildesley, D. J. *Computer Simulation of Liquids*; Clarendon Press: Oxford, UK, 1987.

Allen, P. A.; Allen, J. R. *Basin Analysis: Principles and Applications*. 2nd ed.; Blackwell Pub.: Malden, MA, 2005.

Berendsen, H. J. C.; Postma, J. P. M.; van Gunsteren, W. F.; Hermans, J. Interaction models for water in relation to protein hydration. In *Intermolecular Forces*; Pullmann, B., Ed.; Reidel: Dordrecht, The Netherlands, 1981; 331–342.

Botan, A.; Rotenberg, B.; Marry, V.; Turq, P.; Noetinger, B. Carbon Dioxide in Montmorillonite Clay Hydrates: Thermodynamics, Structure, and Transport from Molecular Simulation. *J. Phys. Chem. C* **2010,** *114*, 14962–14969.

Bourg, I.; Sposito, G. Molecular Dynamics Simulations of the Electrical Double Layer on Smectite Surfaces Contacting Concentrated Mixed Electrolyte (NaCl–$CaCl_2$) Solutions. *J. Colloid. Interface Sci.* **2011,** *360*, 701–715.

Brown, D.W.; Sokol, P.E.; Fitzgerald, S.A. Rotational Dynamics of *n*-H_2 in Porous Vycor Glass. *Phys. Rev. B* **1999,** *59*, 13258–13266.

Cole, D. R.; Chialvo, A. A.; Rother, G.; Vlcek, L.; Cummings, P.T. Supercritical Fluid Behavior at Nanoscale Interfaces: Implications for CO_2 Sequestration in Geologic Formations. *Phil. Magazine* **2010,** *90*, 2339–2363.

Costanzo, P. M. Baseline Studies of the Clay Minerals Society Source Clays: Introduction. *Clays Clay Miner.* **2001,** *49*, 372–373.

CP2K program suite, www.cp2k.org (accessed October 24, 2013).

Cygan, R. T.; Liang, J.-J.; Kalinichev, A. G. Molecular Models of Hydroxide, Oxyhydroxide, and Clay Phases and the Development of a General Force Field. *J. Phys. Chem. B* **2004,** *108*, 1255–1266.

Cygan, R. T.; Romanov, V. N.; Myshakin, E. M. Molecular Simulation of Carbon Dioxide Capture by Montmorillonite Using an Accurate and Flexible Force Field. *J. Phys. Chem. C* **2012,** *116*, 13079−13091.

Cygan, R. T.; Greathouse, J. A.; Heinz, H., Kalinichev, A. G. Molecular Models and Simulations of Layered Materials. *J. Mater. Chem.* **2009,** *19*, 2470–2481.

de Lange, K. M.; Joseph R.; Lane, J. R. Explicit Correlation and Intermolecular Interactions: Investigating Carbon Dioxide Complexes with the CCSD(T)-F12 Method. *J. Chem. Phys.* **2011,** *134*, 034301/1–034301/9.

Ferrage, E.; Kirk, C. A.; Cressey, G.; Cuadros, J. Dehydration of Ca-montmorillonite at the Crystal Scale. Part I: Structure Evolution. *Am. Mineral.* **2007,** *92*, 994–100.

Ferrage, E.; Lanson, B.; Sakharov, B. A.; Drits, V. A. Investigation of Smectite Hydration Properties by Modeling of X-ray Diffraction Profiles. Part 1. Montmorillonite Hydration properties. *Am. Mineral.* **2005,** *90*, 1358–1374.

Fu, M. H.; Zhang, Z. Z.; Low, P. F. Changes in the Properties of a Montmorillonite-Water System during the Adsorption and Desorption of Water: Hysteresis. *Clays Clay Miner.* **1990,** *38*, 485–492.

Garden, A. L.; Lane, J. R.; Kjaergaard, H. G. Counterpoise Corrected Geometries of Hydrated Complexes. *J. Chem. Phys.* **2006,** *125*, 144317/1−144317/6.

Garrett-Roe, S.; Hamm, P. Purely Absorptive Three-dimensional Infrared Spectroscopy. *J. Chem. Phys.* **2009,** *130*, 164510–164519.

Gaus, I. Role and Impact of CO_2–Rock Interactions during CO_2 Storage in Sedimentary Rocks. *Int. J. Greenhouse Gas Control* **2010,** *4*, 73–89.

Giesting, P.; Guggenheim, S.; Koster van Groos, A. F.; Busch, A. Interaction of Carbon Dioxide with Na-exchanged Montmorillonite at Pressures to 640 bars: Implications for CO_2 Sequestration. *Int. J. Greenhouse Gas Control* **2012,** *8*, 73–81.

Goedecker, S.; Teter, M.; Hutter, J. Separable Dual-space Gaussian Pseudopotentials. *Phys. Rev. B* **1996,** *54*, 1703−1710.

Gregoire, G.; Duncan, M. A. Infrared Spectroscopy to Probe Structure and Growth Dynamics in Fe^+-$(CO_2)_n$ Clusters. *J. Chem. Phys.* **2002,** *117*, 2120–2130.

Grimme, S. Semiempirical GGA-type Density Functional Constructed with a Long-range Dispersion Correction. *J. Comput. Chem.* **2006,** *27*, 1787–1799.

Harris, J. G.; Yung, K. H. Carbon Dioxide's Liquid-Vapor Coexistence Curve And Critical Properties as Predicted by a Simple Molecular Model. *J. Phys. Chem.* **1995,** *99*, 12021–12024.

Hoover, W. G. Canonical Dynamics: Equilibrium phase-space Distributions. *Phys. Rev. A* **1985,** *31*, 1695–1697.

Hur, T.-B.; Baltrus, J. P.; Howard, B. H.; Harbert, W. P.; Romanov, V. N. Carbonate Formation in Wyoming Montmorillonite under High Pressure Carbon Dioxide. *Int. J. Greenhouse Gas Control* **2013,** *13*, 149–155.

Ilton, E. S.; Schaef, H. T.; Qafoku, O.; Rosso, K. M.; Felmy, A. R. In Situ X-ray Diffraction Study of Na^+ Saturated Montmorillonite Exposed to Variably Wet Super Critical CO_2. *Environ. Sci. Technol*. **2012,** *46*, 4241−4248.

Jaeger, J. B.; Jaeger, T. D.; Brinkmann, N. R.; Schaefer, H. F.; Duncan, M. A. Infrared Photodissociation Spectroscopy of $Si^+(CO_2)_n$ and $Si^+(CO_2)_nAr$ Complexes: Evidence for Unanticipated Intracluster Reactions. *Can. J. Chem.,* **2004,** *82*, 934–946.

Kono, H.; Ziv, A.R.; Lin, S.H. Theoretical Studies of Molecules Adsorbed on Solid Surfaces: I. Electronic Spectra. *Surface Sci.* **1983,** *134*, 614–638.

Kozaki, T.; Fujishima, A.; Sato, S.; Ohashi, H. Self-Diffusion of Sodium Ions in Compacted Sodium Montmorillonite. *Nucl. Technology* **1998,** *121*, 63–69.

Kozaki, T.; Liu, J.; Sato, S. Diffusion Mechanism of Sodium Ions in Compacted Montmorillonite under Different NaCl Concentration. *Phys. Chem. Earth* **2008,** *33*, 957–961.

Krack, M. Pseudopotentials for H to Kr Optimized for Gradient-corrected Exchange-correlation Functionals. *Theor. Chem. Acc.* **2005,** *114*, 145−152.

Kumar, P. P.; Kalinichev, A. G.; Kirkpatrick, R. G. Hydrogen-Bonding Structure and Dynamics of Aqueous Carbonate Species from Car-Parrinello Molecular Dynamics Simulations. *J. Phys. Chem. B* **2009,** *113,* 794–802.

Kwak, J. H.; Hu, J. Z.; Turcu, R. V. F.; Rosso, K. M.; Ilton, E. S.; Wang, C. M.; Sears, J. A.; Engelhard, M.H.; Felmy, A.R.; Hoyt, D. W. The Role of H_2O in the Carbonation of Forsterite in Supercritical CO_2. *Int. J. Greenhouse Gas Control* **2011,** *5*, 1081–1092.

Lee, J. H.; Guggenheim, S. Single crystal X-ray refinement of pyrophyllite-1T*c. Am. Mineral.* **1981,** *66*, 350–357.

Lindeberg, E. G. B.; Wessel-Berg, D. Vertical Convection in an Aquifer Column under a Gas Cap of CO_2. *Energy Convers. Mgmt.* **1997,** *38*, S229–S234.

Loring, J. S.; Schaef, H. T.; Turcu, R. V. F.; Thompson, C. J.; Miller, Q. R. S.; Martin, P. F.; Hu, J.; Hoyt, D. W.; Qafoku, O.; Ilton, E. S.; Felmy, A. R.; Rosso, K. M. *In Situ* Molecular Spectroscopic Evidence for CO_2 Intercalation into Montmorillonite in Supercritical Carbon Dioxide. *Langmuir* **2012,** *28*, 7125−7128.

Malikova, N.; Cadene, A.; Dubois, E.; Marry, V.; Durand-Vidal, S.; Turq, P.; Breu, J.; Zanotti, J.-M.; Longeville, S. Water Diffusion in a Synthetic Hectorite Clay Studied by Quasi-elastic Neutron Scattering. *J. Phys. Chem. C* **2007,** *111*, 17603–17611.

Marry, V.; Dubois, E.; Malikova, N.; Durand-Vidal, S.; Longeville, S.; Breu, J. Water Dynamics in Hectorite Clays: Influence of Temperature Studied by Coupling Neutron Spin Echo and Molecular Dynamics. *Environ. Sci. Technol.* **2011,** *45*, 2850–2855.

Marry, V.; Malikova, N.; Cadene, A.; Dubois, E.; Durand-Vidal, S.; Turq, P.; Breu, J.; Longeville, S.; Zanotti, J.-M. Water Diffusion in a Synthetic Hectorite by Neutron Scattering—beyond the Isotropic Translational Model. *J. Phys.: Condens. Matter* **2008,** *10*, 104205.

Marry, V.; Turq, P.; Cartailler, T.; Levesque, D. Microscopic Simulation of Structure and Dynamics of Water and Counterions in a Monohydrated Montmorillonite. *J. Chem. Phys.* **2002,** *117*, 3454–3463.

Martin, R. T. Data *Handbook for Clay Materials and Other Non-Metallic Minerals*; van Olphen, H., Fripiat, J. J., Eds.; Pergamon Press, Oxford and Elmsford: New York, NY, 1979.

Marx, D., Hutter. J. *Ab Initio Molecular Dynamics: Basic Theory and Advanced Methods*; Cambridge University Press: Cambridge, UK, 2009.

Moin, S. T.; Pribil, A. B.; Lim, L. H. V.; Hofer, T. S.; Randolf, B. R.; Rode, B. M. Carbon Dioxide in Aqueous Environment—A Quantum Mechanical Charge Field Molecular Dynamics Study. *Int. J. Quant. Chem.* **2011,** *111*, 1370–1378.

NETL. Carbon Storage, www.netl.doe.gov/technologies/carbon_seq/corerd/storage.html (accessed February 15, 2013).

Nóse, S. A Molecular Dynamics Method for Simulations in the Canonical Ensemble. *Mol. Phys.* **1984,** *52*, 255–268.

Nóse, S.; Klein, M. L. Constant Pressure Molecular Dynamics for Molecular Systems. *Mol. Phys.* **1983,** *50*, 1055–1076.

Papousek, D.; Aliev, M. R. *Molecular Vibrational-rotational Spectra: Theory and Applications of High Resolution Infrared, Microwave and Raman Spectroscopy of Polyatomic Molecules*; Elsevier Science Ltd., 1982.

Parrinello, M.; Rahman, A. Polymorphic Transitions in Single Crystals: A New Molecular Dynamics Method. *J. Appl. Phys.* **1981,** *52*, 7182–7190.

Peng, X.; Zhao, J.; Cao, D. J. Adsorption of Carbon Dioxide of 1-Site and 3-Site Models in Pillared Clays: A Gibbs Ensemble Monte Carlo Simulation. *Colloid and Interface Sci.* **2007,** *310*, 391–401.

Perdew, J. P.; Burke, K.; Ernzerhof, M. Generalized Gradient Approximation Made Simple. *Phys. Rev. Lett.* **1996,** *77*, 3865–3868.

Romanov, V. N. Evidence of Irreversible CO_2 Intercalation in Montmorillonite. *Int. J. Greenhouse Gas Control* **2013,** *14*, 220–226.

Romanov, V. N.; Cygan, R. T.; Howard, B. H.; Myshakin, E. M.; Guthrie, G. D. Mechanisms of CO2 Interaction with Expansive Clay. In *Proceedings of the 2010 SEA-CSSJ-CMS Trilateral Meeting on Clays*; Seville, Spain, June 8–10, 2010a.

Romanov, V. N.; Howard, B. H.; Lynn, R. J.; Warzinski, R. P.; Hur, T. B.; Myshakin, E. M.; Lopano, C. L.; Voora, V. K.; Al-Saidi, W. A.; Jordan, K. D.; Cygan, R. T.; Guthrie, G. D. CO_2 Interaction with Geomaterials; American Geophysical Union Fall Meeting, San Francisco, December 13–17, 2010b; H11J01.

Sato, T.; Watanabe, T.; Otsuka, R. Effects of Layer Charge, Charge Location, and Energy Change on Expansion Properties of Dioctahedral Smectites. *Clays and Clay Miner.* **1992,** *40*, 103–113.

Schaef, H. T.; Ilton, E. S.; Qafoku, O.; Martin, P. F.; Felmy, A. R.; Rosso, K. M. *In situ* XRD Study of Ca^{2+} Saturated Montmorillonite (STX-1) Exposed to Anhydrous and Wet Supercritical Carbon Dioxide. *Int. J. Greenhouse Gas Control* **2012,** *6*, 220–229.

Schaffert, J.; Cottin, M.C.; Sonntag, A.; Karacuban, H.; Bobisch, C. A; Lorente, N.; Gauyac, J.-P.; Möller, R. Imaging the Dynamics of Individually Adsorbed Molecules. *Nature Mater. Lett.* **2013,** *12*, 223–227.

Sholl, D.; Steckel, J. A. *Density Functional Theory: A Practical Introduction*; John Wiley & Sons, Inc.: Hoboken, NJ, 2009.

Smith, D. Molecular Computer Simulations of the Swelling Properties and Interlayer Structure of Cesium Montmorillonite. *Langmuir* **1998,** *14*, 5959–5967.

Spycher, N.; Pruess, K.; Ennis-King, J. CO_2-H_2O Mixtures in the Geological Sequestration of CO_2. I. Assessment and Calculation of Mutual Solubilities from 12 to 100 °C and up to 600 bar. *Geochim. et Cosmochim. Acta* **2003,** *67*, 3015–3031.

Thomas, W.; Adams, M. Measurement of the Diffusion Coefficients of Carbon Dioxide and Nitrous Oxide in Water and Aqueous Solutions of Glycerol. *Trans. Faraday Soc.* **1965,** *61*, 668–673.

Tkatchenko, A.; Scheffler, M. Accurate Molecular Van Der Waals Interactions from Ground-State Electron Density and Free-Atom Reference Data. *Phys. Rev. Lett.* **2009,** *102*, 073005–1–073005-4.

van der Spoel, D. ; Lindahl, E.; Hess, B.; van Buuren, A. R.; Apol, E.; Meulenhoff, P. J.; Tieleman, D. P.; Sijbers, A. L. T. M.; Feenstra, K. A.; van Drunen, R.; Berendsen, H. J. C. Gromacs User Manual version 4.5.4, www.gromacs.org (accessed February 15, 2013).

van der Spoel, D.; van Maaren, P. J.; Larsson, P.; Timneanu, N. Thermodynamics of Hydrogen Bonding in Hydrophilic and Hydrophobic Media. *J. Phys. Chem. B* **2006,** *110*, 4393–4398.

van Gunsteren, W.F.; Berendsen, H. J. C. A Leap-frog Algorithm for Stochastic Dynamics. *Mol. Sim.* **1988,** *1*, 173–185.

VandeVondele, J.; Hutter, J. Gaussian Basis Sets for Accurate Calculations on Molecular Systems in Gas and Condensed Phases. *J. Chem. Phys.* **2007,** *127*, 114105–114109.

Vlcek, L.; Chialvo, A. A.; Cole, D. R. Optimized Unlike-Pair Interactions for Water–Carbon Dioxide Mixtures Described by the SPC/E and EPM2 Models. *J. Phys. Chem. B* **2011,** *115*, 8775–8784.

Voora, V. K.; Saidi, W. A.; Jordan, K. D. Private communication, 2013.

Voora, V.K.; Al-Saidi, Jordan, K. D. Density Functional Theory Study of Pyrophyllite and M-Montmorillonites (M = Li, Na, K, Mg, and Ca): Role of Dispersion Interactions. *J. Phys. Chem. A* **2011,** *115*, 9695–9703.

Walker, N. R.; Grieves, G. A.; Walters, R. S.; Duncan, M. A. The Metal Coordination in $Ni^{+}(CO_2)_n$ and $NiO_2^{+}(CO_2)_m$ Complexes. *Chem. Phys. Lett.* **2003,** *380*, 230–236.

Wan, J.; Jung, J.; Kim, Y., Wettability Alternation upon Reaction with CO_2: Silica, Mica, and Calcite; Nanoscale Control of Geologic CO_2 Fall Symposium, Lawrence Berkeley National Laboratory, Berkeley, CA, October 3–4, 2011.

Yang, X.; Zhang, C. Structure and Diffusion Behavior of Dense Carbon Dioxide Fluid in Clay-like Slit Pores by Molecular Dynamics Simulation. *Chem. Phys. Lett.* **2005,** *407*, 427–432.

Yu, Y.; Yang, X. Molecular Simulation of Swelling and Interlayer Structure for Organoclay in Supercritical CO_2. *Phys. Chem. Chem. Phys.* **2011,** *13*, 282–290.

Zhang, G.; Al-Saidi, W. A.; Myshakin, E. M.; Jordan, K. D. Dispersion-Corrected Density Functional Theory and Classical Force Field Calculations of Water Loading on a Pyrophyllite(001) Surface. *J. Phys. Chem. C* **2012,** *116*, 17134–17141.

This page intentionally left blank.

Sean Plasynski
Executive Director
Technology Development & Integration Center
National Energy Technology Laboratory
U.S. Department of Energy

Cynthia Powell
Executive Director
Research & Innovation Center
National Energy Technology Laboratory
U.S. Department of Energy

John Wimer
Associate Director
Strategic Planning
Science & Technology Strategic Plans & Programs
National Energy Technology Laboratory
U.S. Department of Energy

Traci Rodosta
Strategic Planning
Science & Technology Strategic Plans & Programs
National Energy Technology Laboratory
U.S. Department of Energy

Mark Ackiewicz
Director
Division of Carbon Capture and Storage
Office of Fossil Energy
U.S. Department of Energy